

## THE ORIGIN OF THE SPURIOUS IRON SPREAD IN THE GLOBULAR CLUSTER NGC 3201

A. MUCCIARELLI<sup>1</sup>, E. LAPENNA<sup>1</sup>, D. MASSARI<sup>1</sup>, F.R. FERRARO<sup>1</sup>, B. LANZONI<sup>1</sup>

<sup>1</sup>Dipartimento di Fisica & Astronomia, Alma Mater Studiorum, Università di Bologna, Viale Berti Pichat, 6/2 - 40127, Bologna, ITALY  
*Draft version October 24, 2018*

### ABSTRACT

NGC 3201 is a globular cluster suspected to have an intrinsic spread in the iron content. We re-analysed a sample of 21 cluster stars observed with UVES-FLAMES at the Very Large Telescope and for which Simmerer et al. found a 0.4 dex wide [Fe/H] distribution with a metal-poor tail. We confirmed that when spectroscopic gravities are adopted, the derived [Fe/H] distribution spans  $\sim 0.4$  dex. On the other hand, when photometric gravities are used, the metallicity distribution from Fe I lines remains large, while that derived from Fe II lines is narrow and compatible with no iron spread. We demonstrate that the metal-poor component claimed by Simmerer et al. is composed by asymptotic giant branch stars that could be affected by non local thermodynamical equilibrium effects driven by iron overionization. This leads to a decrease of the Fe I abundance, while leaving the Fe II abundance unaltered. A similar finding has been already found in asymptotic giant branch stars of the globular clusters M5 and 47 Tucanae. We conclude that NGC 3201 is a normal cluster, with no evidence of intrinsic iron spread.

*Subject headings:* stars: abundances — techniques: spectroscopic — globular clusters: individual (NGC 3201)

### 1. INTRODUCTION

The striking homogeneity in terms of iron abundance is usually considered as the main chemical signature of globular clusters (GCs), indicating that these stellar systems were not able to retain the gas ejected by supernova (SN) explosions (see e.g. Renzini & Buzzoni 1986; Willman & Strader 2012). For four decades, only one GC-like system, namely  $\omega$  Centauri, was known to display an intrinsic dispersion in Fe (see e.g. Freeman & Rodgers 1975; Norris & Da Costa 1995; Origlia et al. 2003; Johnson & Pilachowski 2010; Pancino et al. 2011) and this evidence brought to classify the system as the remnant core of a tidally disrupted dwarf galaxy accreted by the Milky Way. In the last few years, deep and extensive spectroscopic and photometric investigations have revealed a more complex picture, with the discovery of other (massive) GCs harboring distinct sub-populations with different iron abundance, as Terzan 5 (Ferraro et al. 2009; Origlia et al. 2011, 2013; Massari et al. 2014) and M2 (Yong et al. 2014), or with large but uni-modal iron distributions, as M54 (Carretta et al. 2010a) and M22 (Marino et al. 2009). Further suggestions of intrinsic iron spread are only tentative at the moment, either because based on Ca II lines (NGC5824, Da Costa, Held & Saviane 2014) or because of still disputed results (NGC1851, Carretta et al. 2010b; Villanova et al. 2010).

Among these candidate *anomalous* GCs, the case of NGC 3201 is controversial because different analyses provide conflicting results about its level of iron homogeneity. Gonzalez & Wallerstein (1998) first analysed a sample of CTIO high-resolution spectra of 18 cluster stars, finding large iron variations ( $\Delta[Fe/H] \sim 0.4$  dex). However, an evident trend between [Fe/H] and the effective temperature casts doubts about the reliability of their [Fe/H] distribution. The re-analysis of six of their targets performed by Covey et al. (2003) does not provide additional clues.

Further analyses by Carretta et al. (2009) and Munoz, Geisler & Villanova (2013), based on high-resolution, high signal-to-noise ratio spectra (FLAMES@VLT and MIKE@Magellan, respectively),

do not highlight similar spreads, ruling out large star-to-star variations. On the other hand, Simmerer et al. (2013) analysed UVES@FLAMES and MIKE@Magellan high-resolution spectra of 24 giant stars of the cluster, revealing a metallicity distribution as large as 0.4 dex (not explainable within the uncertainties) and with an evident metal-poor tail (5 out of 24 stars). This iron spread, qualitatively similar to that observed in M22 (Marino et al. 2009), would make NGC 3201 the least massive GC ( $\sim 1.1 \times 10^5 M_{\odot}$ ; McLaughlin & van der Marel 2005) with evidence of SN ejecta retention.

Recently, Lapenna et al. (2014) discovered effects due to the departure from local thermodynamical equilibrium (NLTE) in a sample of asymptotic giant branch (AGB) stars in the globular cluster 47 Tucanae. Such NLTE effects affect the abundances derived from Fe I lines (bringing to an underestimate of 0.1-0.2 dex in [Fe/H]), but leave the abundances from Fe II lines unaltered. On the other hand, red giant branch (RGB) stars do not exhibit similar effects and the abundances from Fe I and Fe II nicely match each other.

Based on this finding, it is well reasonable to ask whether the star-to-star scatter measured in the Fe content of NGC 3201 is genuine or it is due to such a spurious effect, because of the inclusion in the sample of some AGB stars. Note that the NLTE effects can be easily unveiled by comparing the abundances derived from Fe I and Fe II separately.

In this paper we re-analyse the spectra of the stars discussed in Simmerer et al. (2013) in light of the finding by Lapenna et al. (2014). We limit the analysis to the UVES-FLAMES sample, including also the 5 stars populating the metal-poor tail of the Simmerer et al. (2013) distribution.

### 2. OBSERVATIONS

High-resolution spectra taken with UVES-FLAMES@VLT (Pasquini et al. 2000) for 21 giant stars members of NGC 3201 have been retrieved from the ESO archive. The spectra have been acquired with the UVES grating 580 Red Arm CD#3, that provides a high spectral resolution ( $R \sim 45000$ ) and a large spectral coverage ( $\sim 4800$ - $6800$  Å). The spectra have been reduced using the dedicated ESO

pipeline<sup>1</sup>, performing bias subtraction, flat-fielding, wavelength calibration, spectral extraction and order merging. In each exposure one fiber is dedicated to sample the sky background and used to subtract this contribution from each individual spectrum.

Spectroscopic targets have been identified in our photometric catalog, obtained by combining high resolution images acquired with the HST-ACS camera and wide-field images acquired with the ESO-WFI imager. Both the photometric datasets have been obtained through the V and I filters. A total of 13 targets lie in the innermost cluster region, covered by ACS, while 8 stars are in the external region, covered by WFI. The membership of all the targets is confirmed by their very high radial velocity ( $\langle RV_{helio} \rangle = +494.6 \pm 0.8 \text{ km s}^{-1}$ ,  $\sigma = 3.6 \text{ km s}^{-1}$ ) that allows to easily distinguish the cluster members from the surrounding field stars.

The position of the targets in the color-magnitude diagrams (CMDs) is shown in Fig. 1. These CMDs have been corrected for differential reddening using the method described in Massari et al. (2012) and adopting the extinction law by Cardelli, Clayton & Mathis (1989). In order to calculate guess values for the atmospheric parameters of the target stars, we fitted the CMDs with an appropriate theoretical isochrone from the BaSTI dataset (Pietrinferni et al. 2006), computed with an age of 11 Gyr (Marin-Franch et al. 2009),  $Z = 0.001$  and  $\alpha$ -enhanced chemical mixture, finding a color excess  $E(B-V) = 0.31 \text{ mag}$  and a true distance modulus  $(m-M)_0 = 13.35 \text{ mag}$ .

Table 1 lists the main information about the targets, by adopting the same identification numbers used by Simmerer et al. (2013) who adopted the original names by Cote et al. (1994).

### 3. ANALYSIS

Iron abundances have been derived with the package GALA<sup>2</sup> (Mucciarelli et al. 2013a) by matching the measured and theoretical equivalent widths (EWs). Model atmospheres have been calculated with the code ATLAS9<sup>3</sup>. We selected Fe I and Fe II lines predicted to be unblended at the UVES resolution and at the typical atmospheric parameters and metallicity of the observed stars, through the careful inspection of synthetic spectra calculated with the SYNTH package (Sbordone 2005). Atomic data of the transitions of interest are from the last release of the Kurucz/Castelli linelist<sup>4</sup>. The final iron abundances are based on  $\sim 130$ -150 Fe I and  $\sim 15$ -20 Fe II lines. EWs have been measured with DAOSPEC (Stetson & Pancino 2008), run iteratively by means of the package 4DAO<sup>5</sup> (Mucciarelli 2013). EW, oscillator strength and excitation potential for all the measured transitions are listed in Table 2 (available in its entirety in the online version).

#### 3.1. Analysis with spectroscopic gravities

First, we performed a fully spectroscopic analysis, as done by Simmerer et al. (2013), in order to verify whether we obtain the same evidence of a metallicity dispersion. In this analysis the atmospheric parameters have been constrained as follows: (a) for the effective temperatures ( $T_{\text{eff}}$ ) we requested

that no trend exists between abundances and excitation potential, (b) for the surface gravities ( $\log g$ ) we imposed that the same abundance is obtained (within the uncertainties) from Fe I and Fe II lines, (c) for the microturbulent velocity ( $v_{\text{turb}}$ ) we requested that no trend exists between abundances from Fe I lines and the reduced line strength. The derived values of  $v_{\text{turb}}$  are based on  $\sim 130$ -150 Fe I lines distributed over a large interval of reduced EWs, with  $\log(\text{EW}/\lambda)$  ranging between  $-5.6$  and  $-4.7$ .

We derived an average  $[\text{Fe I}/\text{H}] = -1.46 \pm 0.02 \text{ dex}$  ( $\sigma = 0.10 \text{ dex}$ ), with a distribution ranging from  $-1.62 \text{ dex}$  to  $-1.27 \text{ dex}$ . The  $[\text{Fe I}/\text{H}]$  and  $[\text{Fe II}/\text{H}]$  abundance distributions are shown in Fig. 2 as generalized histograms. This result well matches that obtained by Simmerer et al. (2013) that find an average abundance  $[\text{Fe}/\text{H}] = -1.48 \pm 0.02 \text{ dex}$  ( $\sigma = 0.11 \text{ dex}$ )<sup>6</sup> with a comparable iron range ( $\Delta[\text{Fe}/\text{H}] \sim 0.4 \text{ dex}$ ). This spectroscopic analysis fully confirms the claim by Simmerer et al. (2013): when analysed with atmospheric parameters derived following the constraints listed above, the stars of NGC 3201 reveal a clear star-to-star scatter in the iron content. The 5 stars labelled as *metal-poor* by Simmerer et al. (2013), with  $[\text{Fe}/\text{H}] < -1.58 \text{ dex}$ , are the most metal-poor also in our metallicity distribution.

#### 3.2. Analysis with photometric gravities

As pointed out by Lapenna et al. (2014), possible NLTE effects in AGB stars can be easily detected by assuming photometric values for  $\log g$  and measuring Fe I and Fe II independently<sup>7</sup>. In order to see whether this effect is present in the NGC 3201 data, we adopted the following procedure.  $T_{\text{eff}}$  has been derived spectroscopically, by imposing the excitation equilibrium as described above. Thanks to the high quality of the spectra (with S/N ratio per pixel higher than 100) and the large number of Fe I lines distributed over a large range of excitation potentials, very accurate spectroscopic  $T_{\text{eff}}$  can be estimated, with internal uncertainties of about 20-30 K. As a guess value we adopted  $T_{\text{eff}}$  calculated from the  $(V-I)_0 - T_{\text{eff}}$  calibration by Alonso et al. (1999) and assuming a color excess  $E(B-V) = 0.31 \text{ mag}$ . Gravities have been derived from the Stefan-Boltzmann equation, assuming  $E(B-V) = 0.31 \text{ mag}$ ,  $(m-M)_0 = 13.35 \text{ mag}$ , bolometric corrections from Alonso et al. (1999) and a mass of  $0.82 M_{\odot}$  (according to the best-fit isochrone, the latter is a suitable value for RGB stars brighter than the RGB Bump magnitude level). Because  $T_{\text{eff}}$  is derived spectroscopically, the gravity is recomputed through the Stefan-Boltzmann equation in each iteration according to the new value of  $T_{\text{eff}}$ . The mass value of  $0.82 M_{\odot}$  is appropriate for RGB stars but probably too high for AGB stars, because of mass loss phenomena during the RGB phase (Rood 1973; Origlia et al. 2002, 2007, 2014). In

<sup>6</sup> Note that Simmerer et al. (2013) adopted as solar reference value 7.56 obtained from their own solar analysis, while we used 7.50 by Grevesse & Sauval (1998). Throughout the paper we refer to the abundances by Simmerer et al. (2013) corrected for the different solar zero-point.

<sup>7</sup> Recently, Johnson et al. (2014) analysed a sample of 35 AGB stars in 47 Tucanae, finding no clear evidence of NLTE effects. Even if a detailed comparison between the two analyses is not the scope of this paper, we highlight some main differences between the two works: the spectral resolution (48000 in Lapenna et al. (2014) and 22000 in Johnson et al. 2014), the number of Fe II lines (13 in Lapenna et al. (2014) and 4 in Johnson et al. 2014, , on average) and the adopted linelists for AGB and RGB stars (Lapenna et al. (2014) adopted the same linelist for both the groups of stars, at variance with Johnson et al. (2014) that used a linelist consistent, but not exactly the same, with that adopted by Cordero et al. (2014) where the reference RGB stars are discussed).

<sup>1</sup> <http://www.eso.org/sci/software/pipelines/>

<sup>2</sup> <http://www.cosmic-lab.eu/gala/gala.php>

<sup>3</sup> <http://wwwuser.oats.inaf.it/castelli/sources/atlas9codes.html>

<sup>4</sup> <http://wwwuser.oats.inaf.it/castelli/linelists.html>

<sup>5</sup> <http://www.cosmic-lab.eu/4dao/4dao.php>

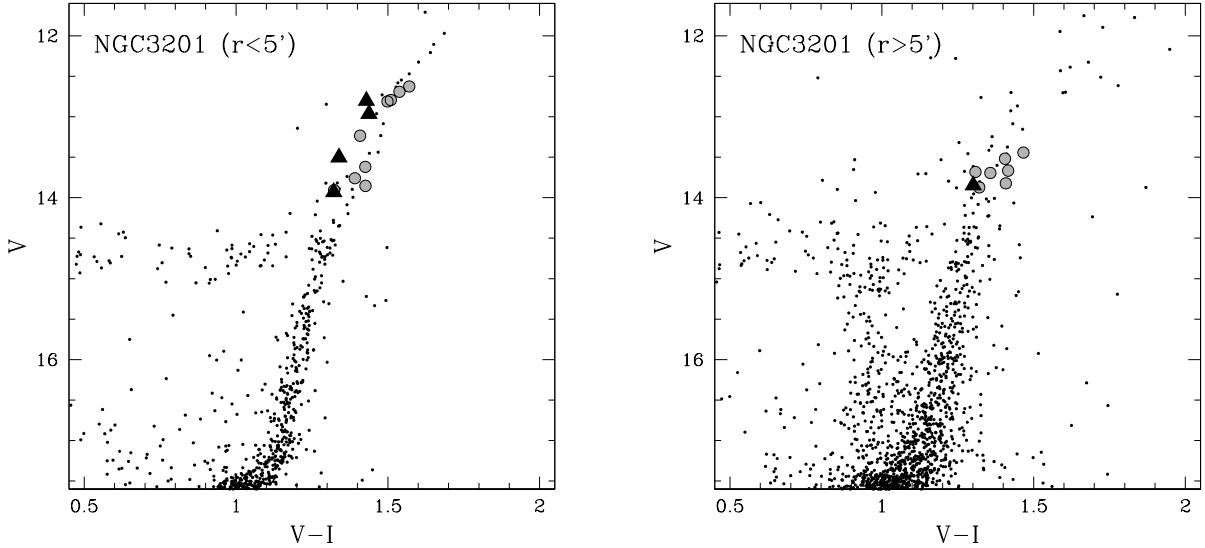


FIG. 1.— CMDs for central and external regions of NGC 3201 (left and right panels, respectively), corrected for differential reddening. Large circles are the spectroscopic targets flagged as *metal-rich* ( $[\text{Fe}/\text{H}] > -1.58$  dex) in Simmerer et al. (2013), while large triangles those identified as *metal-poor* ( $[\text{Fe}/\text{H}] \leq -1.58$  dex).

TABLE 1

Star	RA (J2000)	Dec (J2000)	V	I	$RV_{\text{helio}}$ (km/s)	$T_{\text{eff}}$ (K)	$\log g$	$v_{\text{turb}}$ (km/s)	[Fe I/H] (dex)	[Fe II/H] (dex)
63	154.3084680	-46.4125790	13.76	12.42	495.9±0.6	4730	1.54	1.45	-1.27±0.03	-1.35±0.05
89	154.3346190	-46.3860090	13.87	12.56	498.8±0.5	4855	1.63	1.60	-1.57±0.02	-1.35±0.03
91	154.3359600	-46.3355290	13.81	12.41	490.4±0.6	4705	1.56	1.50	-1.36±0.05	-1.35±0.05
105	154.3439854	-46.4201000	13.94	12.59	493.9±0.9	4760	1.61	1.45	-1.31±0.03	-1.29±0.05
124	154.3601786	-46.4140432	12.85	11.32	498.5±0.2	4375	0.96	1.55	-1.37±0.02	-1.40±0.05
129	154.3623900	-46.4312480	13.54	12.13	491.8±0.4	4580	1.36	1.50	-1.48±0.02	-1.43±0.04
181	154.3876490	-46.4126379	13.89	12.58	497.5±0.4	4920	1.65	1.65	-1.62±0.03	-1.37±0.04
200	154.3949420	-46.3972062	12.79	11.30	495.1±0.4	4515	0.99	1.85	-1.50±0.02	-1.40±0.04
222	154.4031199	-46.4257714	12.69	11.15	491.0±0.5	4355	0.88	1.65	-1.47±0.02	-1.45±0.05
231	154.4067690	-46.4012923	13.52	12.18	491.2±0.5	4785	1.45	1.60	-1.54±0.02	-1.39±0.03
240	154.4091582	-46.4277707	13.91	12.59	495.2±0.6	4855	1.64	1.55	-1.61±0.03	-1.38±0.04
244	154.4097946	-46.4024205	13.77	12.38	492.2±0.3	4690	1.51	1.50	-1.44±0.02	-1.44±0.05
249	154.4104867	-46.4270988	12.99	11.54	498.1±0.3	4545	1.11	1.60	-1.56±0.02	-1.42±0.04
277	154.4198397	-46.4124756	13.60	12.18	497.6±0.3	4620	1.39	1.50	-1.40±0.02	-1.42±0.05
279	154.4208433	-46.3954964	13.34	11.89	499.0±0.3	4555	1.26	1.50	-1.43±0.03	-1.43±0.04
303	154.4288640	-46.3800960	13.58	12.20	491.7±0.4	4630	1.39	1.50	-1.45±0.02	-1.45±0.04
308	154.4304349	-46.4108231	13.76	12.37	487.2±0.4	4620	1.45	1.45	-1.50±0.02	-1.45±0.04
312	154.4342122	-46.4240651	12.71	11.10	494.9±0.3	4330	0.85	1.65	-1.44±0.03	-1.44±0.06
332	154.4478331	-46.3982898	12.96	11.47	499.7±0.5	4500	1.08	1.65	-1.54±0.02	-1.38±0.04
344	154.4544130	-46.4162830	13.82	12.41	490.7±0.7	4655	1.49	1.40	-1.31±0.03	-1.29±0.05
374	154.5004800	-46.5194470	13.64	12.09	498.7±0.6	4595	1.38	1.50	-1.41±0.03	-1.36±0.05
									$\langle [\text{Fe I}/\text{H}] \rangle$	$\langle [\text{Fe II}/\text{H}] \rangle$
									-1.46±0.02	-1.40±0.01

NOTE. — Main information of the target stars. Identification numbers are the same adopted by Simmerer et al. (2013). [Fe I/H] and [Fe II/H] have been obtained adopting photometric gravities.

fact, Gratton et al. (2010) provide the masses for a sample of HB stars in NGC 3201, finding values between 0.62 and 0.71  $M_{\odot}$ . We initially analysed all the targets assuming the mass of a RGB star. Then, the AGB candidates, selected according to their position in  $T_{\text{eff}}-\log g$  plane (as discussed in Section 4) have been re-analysed by assuming the median value (0.68  $M_{\odot}$ ) of the HB stars estimated by Gratton et al. (2010).

This method allows us to take advantage of the high-quality of the spectra, deriving accurate  $T_{\text{eff}}$  thanks to the large number of transitions spanning a large range of excitation potentials. On the other hand, this approach does not require a fully spectroscopic determination of  $\log g$  that is instead calculated using both photometric information and spectroscopic

$T_{\text{eff}}$ , avoiding any possible bias related to NLTE effects.

The [Fe I/H] and [Fe II/H] abundances obtained with this method are listed in Table 1. The right panel of Fig. 2 shows the [Fe I/H] and [Fe II/H] distributions represented as generalized histograms obtained from this analysis. The two distributions turn out to be quite different. The iron distribution obtained from Fe I lines resembles that obtained with the spectroscopic parameters (left panel of Fig. 2), with an average value of  $[\text{Fe I}/\text{H}] = -1.46 \pm 0.02$  dex ( $\sigma = 0.10$  dex), while the distribution obtained from Fe II lines has a narrow gaussian shape ( $[\text{Fe II}/\text{H}] > -1.40 \pm 0.01$  dex,  $\sigma = 0.05$  dex) pointing to a quite homogeneous iron content.

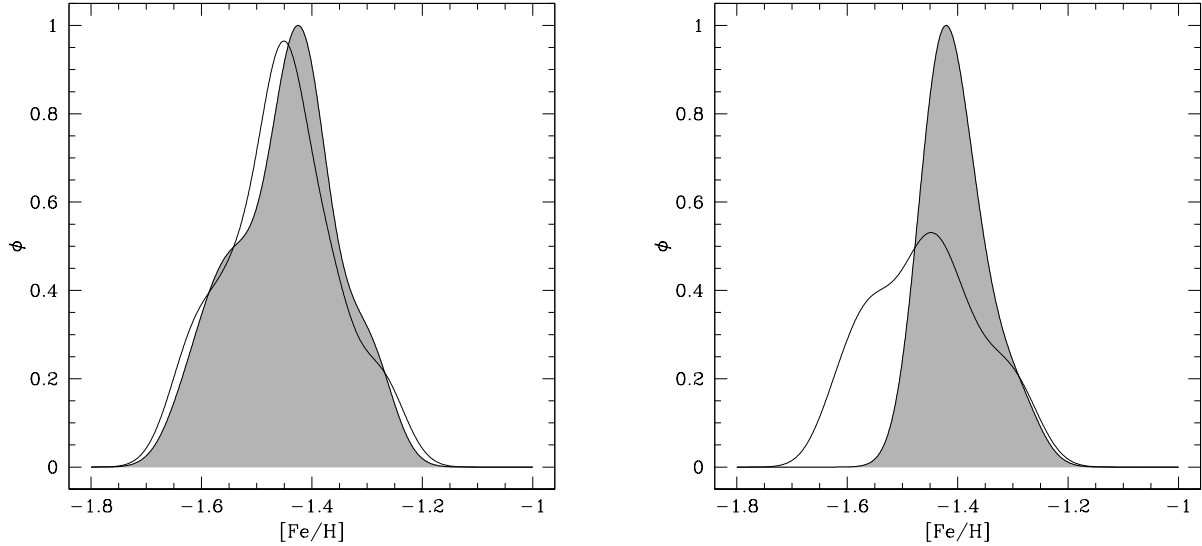


FIG. 2.— Generalized histograms for [Fe I/H] (empty histogram) and [Fe II/H] (grey histogram) obtained from the analysis performed with spectroscopic gravities (left panel) and with photometric gravities (right panel).

TABLE 2  
STAR IDENTIFICATION NUMBER, WAVELENGTH,  
OSCILLATOR STRENGTH, EXCITATION POTENTIAL  
AND MEASURED EWs FOR ALL THE USED  
TRANSITIONS.

Star	$\lambda$ ( $\text{\AA}$ )	Ion	$\log(gf)$	E.P. (eV)	EW (m $\text{\AA}$ )
63	4791.246	Fe I	-2.435	3.270	26.40
63	4834.507	Fe I	-3.330	2.420	27.90
63	4842.788	Fe I	-1.530	4.100	16.30
63	4892.859	Fe I	-1.290	4.220	29.50
63	4911.779	Fe I	-1.760	3.930	19.50
63	4917.230	Fe I	-1.160	4.190	35.90
63	4918.013	Fe I	-1.340	4.230	28.30
63	4950.106	Fe I	-1.670	3.420	54.10
63	4962.572	Fe I	-1.182	4.180	32.30
63	4969.917	Fe I	-0.710	4.220	46.00
63	4985.253	Fe I	-0.560	3.930	75.30
63	5002.793	Fe I	-1.530	3.400	67.20
63	5014.942	Fe I	-0.303	3.940	86.70
63	5022.236	Fe I	-0.560	3.980	76.40
63	5028.126	Fe I	-1.123	3.570	68.30

NOTE. — This table is available in its entirety in a machine-readable form in the online journal. A portion is shown here for guidance regarding its form and content.

### 3.3. Uncertainties

Internal uncertainties in the derived Fe abundances have been calculated by adding in quadrature two sources of uncertainties:

(1) those arising from the EW measurement. For each target, we estimated this term as the line-to-line dispersion normalized to the root mean square of the number of lines. Because of the high quality of the used spectra, the line-to-line scatters are smaller than 0.1 dex, leading to internal uncertainties of about 0.005-0.008 dex for [Fe I/H] and of about 0.010-0.025 dex for [Fe II/H].

(2) those arising from the atmospheric parameters. To estimate this term, we follow the approach described by Cayrel et al. (2004) to take into account the covariance terms due to the correlations among the atmospheric param-

TABLE 3  
ABUNDANCE UNCERTAINTIES DUE TO THE  
ATMOSPHERIC PARAMETERS FOR THE STARS #63 AND  
#89.

Ion	Parameters Uncertainty (dex)	$\delta T_{\text{eff}}$ $\pm 50$ K (dex)	$\delta \log g$ $\pm 0.1$ (dex)	$\delta v_{\text{turb}}$ $\pm 0.1$ km/s (dex)
#63 (RGB)				
Fe I	$\pm 0.03$	$\pm 0.05$	$\pm 0.00$	$\mp 0.03$
Fe II	$\pm 0.04$	$\mp 0.02$	$\pm 0.04$	$\pm 0.03$
#89 (AGB)				
Fe I	$\pm 0.02$	$\pm 0.04$	$\pm 0.00$	$\mp 0.03$
Fe II	$\pm 0.03$	$\mp 0.02$	$\pm 0.04$	$\pm 0.02$

NOTE. — The second column is the total uncertainty calculated according to Cayrel et al. (2004). The other columns list the abundance variations related to the variation of only one parameter.

ters. For each target, the temperature has been varied by  $\pm 1\sigma_{T_{\text{eff}}}$ , the gravity has been re-calculated through the Stefan-Boltzmann equation adopting the new values of  $T_{\text{eff}}$  and the microturbulent velocity re-optimized spectroscopically.

Table 1 lists the total uncertainty including both the terms (1) and (2). Also, Table 3 shows for two representative targets (one RGB and one AGB star) the abundance uncertainty obtained following the prescriptions by Cayrel et al. (2004) (second column) and those obtained with the usual method of independently varying each parameter (an approach that obviously does not take into account the correlation among the parameters and can over-estimate the total uncertainty).

## 4. DISCUSSION

In this paper we present a new analysis of the UVES-FLAMES spectra of 21 member stars of NGC 3201 already discussed in Simmerer et al. (2013). The Fe abundances have been calculated both using spectroscopic gravities (obtained by imposing the ionization balance between Fe I and Fe II abundances) and photometric ones (obtained through the Stefan-Boltzmann equation). The two methods provide different results concerning [Fe I/H] and [Fe II/H]. In particular, the use of spectroscopic  $\log g$  provides a wide [Fe/H] distribution (al large as  $\sim 0.4$  dex), in agreement with the finding of

Simmerer et al. (2013) who adopted the same method. On the other hand, when photometric gravities are used, the [Fe I/H] distribution remains quite large, while that of [Fe II/H] is narrow. We compute the intrinsic spread of the two Fe distributions adopting the Maximum Likelihood algorithm described in Mucciarelli et al. (2012). Concerning [Fe I/H] we derive  $\sigma_{int} = 0.09 \pm 0.01$  dex, while for [Fe II/H]  $\sigma_{int} = 0.00 \pm 0.02$  dex. Hence, the [Fe II/H] distribution is compatible with no iron spread.

Simmerer et al. (2013) highlight that the 5 most metal-poor stars of their sample are bluer than the other stars, as expected in cases of a lower metallicity. The left panel of Fig. 3 shows the position of the targets in the  $T_{\text{eff}} - \log g$  plane, with superimposed, as reference, two isochrones with the same age but different metallicity:  $Z = 0.001$  (solid line) and  $Z = 0.0006$  (dashed line). The RGB of the isochrone with  $Z = 0.0006$  overlaps the position of the AGB of the  $Z = 0.001$  isochrone. Seven targets (including the 5 candidate metal-poor stars) are located in a position compatible with both the scenarios: metal-poorer RGB or AGB at the cluster metallicity. These seven targets have average abundances of [Fe I/H] =  $-1.57 \pm 0.01$  dex and [Fe II/H] =  $-1.41 \pm 0.01$  dex, while the RGB stars have [Fe I/H] =  $-1.42 \pm 0.02$  dex and [Fe II/H] =  $-1.40 \pm 0.01$  dex.

However, if these stars were metal-poor RGB stars, the iron abundance derived from Fe I lines should be in agreement with that obtained from Fe II, since NLTE effects are not observed in RGB stars of comparable luminosity and metallicity. The right panel of Fig. 3 shows the behaviour of ([Fe I/H] - [Fe II/H]) as a function of the difference between the spectroscopic values of  $T_{\text{eff}}$  and those obtained from the projection along the RGB of the best-fit isochrone. The stars located along the RGB ( $\Delta T_{\text{eff}} \sim 0$ ) have similar [Fe I/H] and [Fe II/H] abundances, compatible with no NLTE effects. The stars hotter than the reference RGB have differences between [Fe I/H] and [Fe II/H] ranging from  $-0.07$  to  $-0.22$  dex, with a mean value of  $-0.15$  dex. The grey region marks the expected position for metal-poorer RGB stars: they should be hotter than the reference RGB, but with [Fe I/H] - [Fe II/H]  $\sim 0$ , as commonly measured in the RGB stars. This reveals the true nature of these stars: they are genuine AGB stars, with the same metallicity of the cluster (as measured from their Fe II lines) but affected by NLTE effects leading to a systematic decrease of [Fe I/H]. This is the same effect observed by Ivans et al. (2001) and Lapenna et al. (2014) in the AGB stars of M5 and 47 Tucanae, respectively.

A direct inspection of the spectra reveals the different behaviour of Fe I and Fe II lines in AGB and RGB stars. Fig. 4 shows three Fe I lines (chosen with different excitation potential) and one Fe II line in the spectra of the AGB star #89 (upper panels) and of the RGB star #303 (lower panels). Synthetic spectra calculated with the appropriate atmospheric parameters and the metallicity derived from Fe II lines (red lines). In the upper panels we also show the synthetic spectrum computed with the average [Fe I/H] (blue dashed line). Clearly, the synthetic spectrum assuming the [Fe II/H] abundance well reproduces all the observed lines in the case of the RGB star, while it fails to fit the Fe I lines observed in the AGB star, regardless of the excitation potential (pointing out that this effect cannot be attributed to inadequacies in the adopted  $T_{\text{eff}}$ ). On the other hand, the abundance derived from Fe I lines is too low to well reproduce the depth of the AGB Fe II line plotted in Fig. 4. This clearly demonstrates a different behaviour of iron lines in AGB and RGB stars.

It is worth noting that this behaviour is somewhat puzzling, because theoretical models do not predict significant differences in the NLTE corrections for stars in the parameter space covered by our targets. For instance, the grid of NLTE corrections computed by Bergemann et al. (2012) and Lind et al. (2012) predicts that the Fe I lines in AGB and RGB stars should be affected in a very similar way at the metallicity of NGC 3201. However, some additional effects/mechanisms could play a role in the AGB photospheres, leading to the departure from the LTE condition, which are not yet accounted for in the available theoretical calculations.

We checked whether the mass assumed for AGB stars could change our conclusions. The mass distribution of HB stars in NGC 3201 provided by Gratton et al. (2010) ranges from 0.62 to  $0.71 M_{\odot}$ , with a median value of  $0.68 M_{\odot}$ . The minimum and maximum mass values correspond to a difference in  $\log g$  of 0.06, leading to a variation in [Fe II/H] of only 0.02-0.025 dex (and a variation in [Fe I/H] of 0.002-0.005 dex). On the other hand, if we adopt the RGB mass ( $0.82 M_{\odot}$ ) for all targets, as it is often done because of the difficulty to observationally distinguish between RGB and AGB stars, the values of [Fe II/H] increase by only 0.03 dex with respect to estimate obtained assuming  $0.68 M_{\odot}$ . Hence, the precise value of the adopted mass (within a reasonable mass range) cannot reconcile the difference between [Fe I/H] and [Fe II/H].

As additional check, for each AGB stars, the stellar mass has been varied until the ionization equilibrium was satisfied. The derived values range from  $\sim 0.2$  and  $\sim 0.5 M_{\odot}$ : such masses are too low with respect to the mass distribution of the HB stars derived by Gratton et al. (2010). In particular, for the stars #89, #181 and #240, that exhibit the largest difference between [Fe I/H] and [Fe II/H] ( $\sim -0.2$  dex), a satisfying ionization equilibrium can be reached only with masses smaller than 0.2-0.25  $M_{\odot}$ , which are very unlikely values for globular cluster AGB stars.

## 5. CONCLUSIONS

We demonstrated that the observed intrinsic star-to-star Fe scatter in the GC NGC 3201 is due to unaccounted NLTE effects in the spectroscopic analysis of some AGB stars included in the sample. These stars suffer from NLTE effects driven by the iron overionization, a mechanism that affects mainly the less abundant species like Fe I, but has no significant effect on the dominant species (e.g. Fe II). When the gravity of these stars is obtained spectroscopically, forcing to have the same abundance from Fe I and Fe II lines, the derived [Fe/H] abundance turns out to be under-estimated.

Our findings confirm the conclusion by Lapenna et al. (2014) that the chemical analysis of samples of stars including both AGB and RGB stars, and based on spectroscopic gravities, can lead to spurious broadening of the iron distribution.

*We conclude that NGC 3201 is a normal GC, without evidence of intrinsic iron scatter.* In light of this result, it is not necessary to suppose that NGC 3201 was more massive in the past to retain the SN ejecta, as invoked by Simmerer et al. (2013).

We warmly thank the anonymous referee for suggestions that helped improving the paper. This research is part of the project COSMIC-LAB (<http://www.cosmic-lab.eu>) funded by the European Research Council (under contract ERC-2010-AdG-267675).

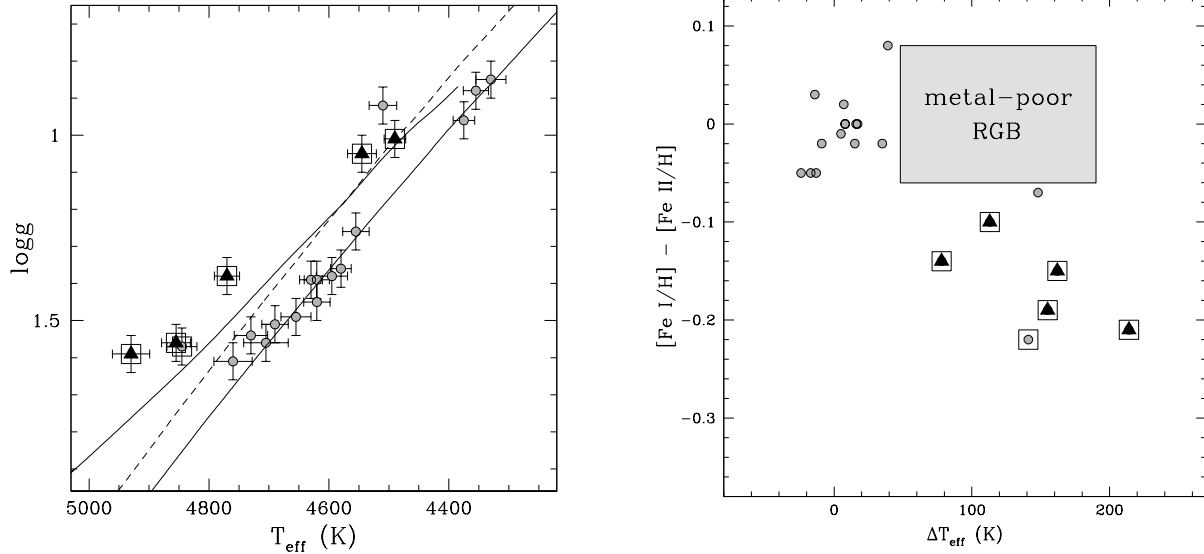


FIG. 3.— *Left panel*: position of the targets in the  $T_{\text{eff}}-\log g$  plane. A BaSTI isochrone with age of 11 Gyr,  $Z=0.001$  and  $\alpha$ -enhancement chemical mixture (solid line) is superimposed for sake of comparison. The dashed line indicates the position of the RGB for a BaSTI isochrone with age of 11 Gyr and  $Z=0.0006$ . Grey triangles are the metal-poor stars of Simmerer et al. (2013). Empty grey squares are the stars in our analysis with  $[\text{Fe I}/\text{H}] - [\text{Fe II}/\text{H}] < -0.1$  dex. *Right panel*: Behaviour of  $[\text{Fe I}/\text{H}] - [\text{Fe II}/\text{H}]$  as a function of the difference between the spectroscopic temperature of each target and the photometric value estimate from the isochrone with  $Z=0.001$  shown in the left panel. Same symbols as in the left panel. The grey light area indicates the expected mean locus for metal-poor ( $[\text{Fe}/\text{H}] \sim -1.6$  dex) RGB stars.

## REFERENCES

- Alonso, A., Arribas, S., & Martínez-Roger, C. 1999, *A&AS*, 140, 261  
 Bergemann, M., Lind, K., Collet, R., Magic, Z., & Asplund, M., 2012, *MNRAS*, 427, 27  
 Cardelli, J. A., Clayton, G. C., & Mathis, J. S., 1989, *ApJ*, 345, 245  
 Carretta, E., Bragaglia, A., Gratton, R., D’Orazi, V., & Lucatello, S., 2009a, *A&A*, 505, 139  
 Carretta, E., Bragaglia, A., Gratton, R. G., Lucatello, S., Bellazzini, M., Catanzaro, G., Leone, F., Momany, Y., Piotto, G., & D’Orazi, V., 2010, *ApJ*, 714L, 7  
 Carretta, E., Gratton, R. G., Lucatello, S., Bragaglia, A., Catanzaro, G., Leone, F., Momany, Y., D’Orazi, V., Cassisi, S., D’Antona, F., & Ortolani S., 2010, *ApJ*, 722L, 1  
 Cayrel, R., Depagne, E., Spite, M., et al., 2004, *A&A*, 416, 1117  
 Cordero, M. J., Pilachowski, C. A., Johnson, C. I., McDonald, I., Zijlstra, A. A., & Simmerer, J., 2014, *ApJ*, 780, 94  
 Cote, P., Welch, D. L., Fischer, P., Da Costa, G. S., Tamblyn, P., Seitzer, P., & Irwin, M. J., 1994, *ApJS*, 90, 83  
 Covey, K. R., Wallerstein, G., Gonzalez, G., Vanture, A. D., & Suntzeff, N. B., 2003, *PASP*, 115, 819  
 Da Costa, G. S., Held, E. V., & Saviane, I., 2014, *MNRAS*, 438, 3507  
 Ferraro, F. R., Dalessandro, E., Mucciarelli, A., Beccari, G., Rich, R. M., Origlia, L., Lanzoni, B., Rood, R. T., Valenti, E., Bellazzini, M., Ransom, S. M., & Cocozza, G., 2009, *Nature*, 462, 483  
 Freeman, K. C., & Rodgers, A. W., 1975, *ApJ*, 201, 71  
 Gonzalez, G. & Wallerstein, G., 1998, *AJ*, 116, 765  
 Gratton, R. G., Carretta, E., Bragaglia, A., Lucatello, S. & D’Orazi, V., 2010, *A&A*, 517, 81  
 Grevesse, N., & Sauval, A. J., 1998, *SSRv*, 85, 161  
 Ivans, I. I., Kraft, R. P., Sneden, C., et al. 2001, *AJ*, 122, 1438  
 Johnson, C. I., & Pilachowski, C. A., 2010, *ApJ*, 722, 1373  
 Johnson, C. I., McDonald, I., Pilachowski, C. A., Mateo, M., Bailly J. I., III, Cordero, M. J., Zijlstra, A. A., Crane, J. D., Olszewski, E., Schectman, S. A., & Thompson, I., 2014, arXiv:1412.4108  
 Lapenna, E., Mucciarelli, A., Lanzoni, B., Ferraro, F. R., Dalessandro, E., Origlia, L., & Massari, D., 2014, *ApJ*, 797, 124  
 Lind, K., Bergemann, M. & Asplund, M., 2012, *MNRAS*, 427, 50  
 Marin-Franch, A., et al., 2009, *ApJ*, 694, 1498  
 Marino, A. F., Milone, A. P., Piotto, G., Villanova, S., Bedin, L. R., Bellini, A., & Renzini, A., 2009, *A&A*, 505, 1099  
 Massari, D., Mucciarelli, A., Dalessandro, E., Ferraro, F. R., Origlia, L., Lanzoni, B., Beccari, G., Rich, R. M., Valenti, E. & Ransom, S. M., 2012, *ApJ*, 755L, 32  
 Massari, D., Mucciarelli, A., Ferraro, F. R., Origlia, L., Rich, R. M., Lanzoni, B., Dalessandro, E., Valenti, E., Ibata, R., Lovisi, L., Bellazzini, M., & Reitzel, D., 2014, *ApJ*, 795, 22  
 McLaughlin, D. E., & van der Marel, R. P., 2005, *ApJS*, 161, 304  
 Mucciarelli, A., Bellazzini, M., Ibata, R., Merle, T., Chapman, S. C., Dalessandro, E., & Sollima, A., 2012, *MNRAS*, 426, 2889  
 Mucciarelli, A., Pancino, E., Lovisi, L., Ferraro, F. R., & Lapenna, E. 2013, *ApJ*, 766, 78  
 Mucciarelli, A. 2013, arXiv:1311.1403  
 Munoz, C., Geisler, D., & Villanova, S., 2013, *MNRAS*, 433, 2006  
 Norris, J. E., & Da Costa, G. S., 1995, *ApJ*, 447, 680  
 Origlia, L., Ferraro, F. R., Fusi Pecci, F. & Rood, R. T., 2002, *ApJ*, 571, 458  
 Origlia, L., Ferraro, F. R., Bellazzini, M., & Pancino, E., 2003, *ApJ*, 591, 916  
 Origlia, L., Rood, R. T., Fabbri, S., Ferraro, F. R., Fusi Pecci, F., & Rich, R. M., 2007, *ApJ*, 667L, 85  
 Origlia, L., Rich, R. M., Ferraro, F. R., Lanzoni, B., Bellazzini, M., Dalessandro, E., Mucciarelli, A., Valenti, E., & Beccari, G., 2011, *ApJ*, 726L, 20  
 Origlia, L., Massari, D., Rich, R. M., Mucciarelli, A., Ferraro, F. R., Dalessandro, E., & Lanzoni, B., 2013, *ApJ*, 779L, 5  
 Origlia, L., Ferraro, F. R., Fabbri, S., Fusi Pecci, F., Dalessandro, E., Rich, R. M., & Valenti, E., 2014, *A&A*, 564, 136  
 Pancino, E., Mucciarelli, A., Sbordone, L., Bellazzini, M., Pasquini, L., Monaco, L. & Ferraro, F. R., 2011, *A&A*, 527, 18  
 Pasquini, L., et al., 2000, *SPIE*, 4008, 129  
 Pietrinferni, A., Cassisi, S., Salaris, M. & Castelli, F., 2006, *ApJ*, 642, 797  
 Renzini, A., & Buzzoni, A., 1986, *Spectral Evolution of Galaxies*, 122, 195  
 Rood, R. T., 1973, *ApJ*, 184, 815  
 Sbordone, L., 2005, *MSAIS*, 8, 61  
 Simmerer, J., Ivans, I. I., Filler, D., Francois, P., Charbonnel, C., Monier, R., & James, G., 2013, *ApJ*, 764L, 7  
 Stetson, P. B., & Pancino, E., *PASP*, 120, 1332  
 Villanova, S., Geisler, D., & Piotto, G., 2010, *ApJ*, 722L, 18  
 Yong, D., Roederer, I. U., Grundahl, F., Da Costa, G. S., Karakas, A. I., Norris, J. E., Aoki, W., Fishlock, C. K., Marino, A. F., Milone, A. P., & Shingles, L. J., 2014, *MNRAS*, 441, 3396  
 Willman, B. & Strader, J., 2012, *AJ*, 144, 76

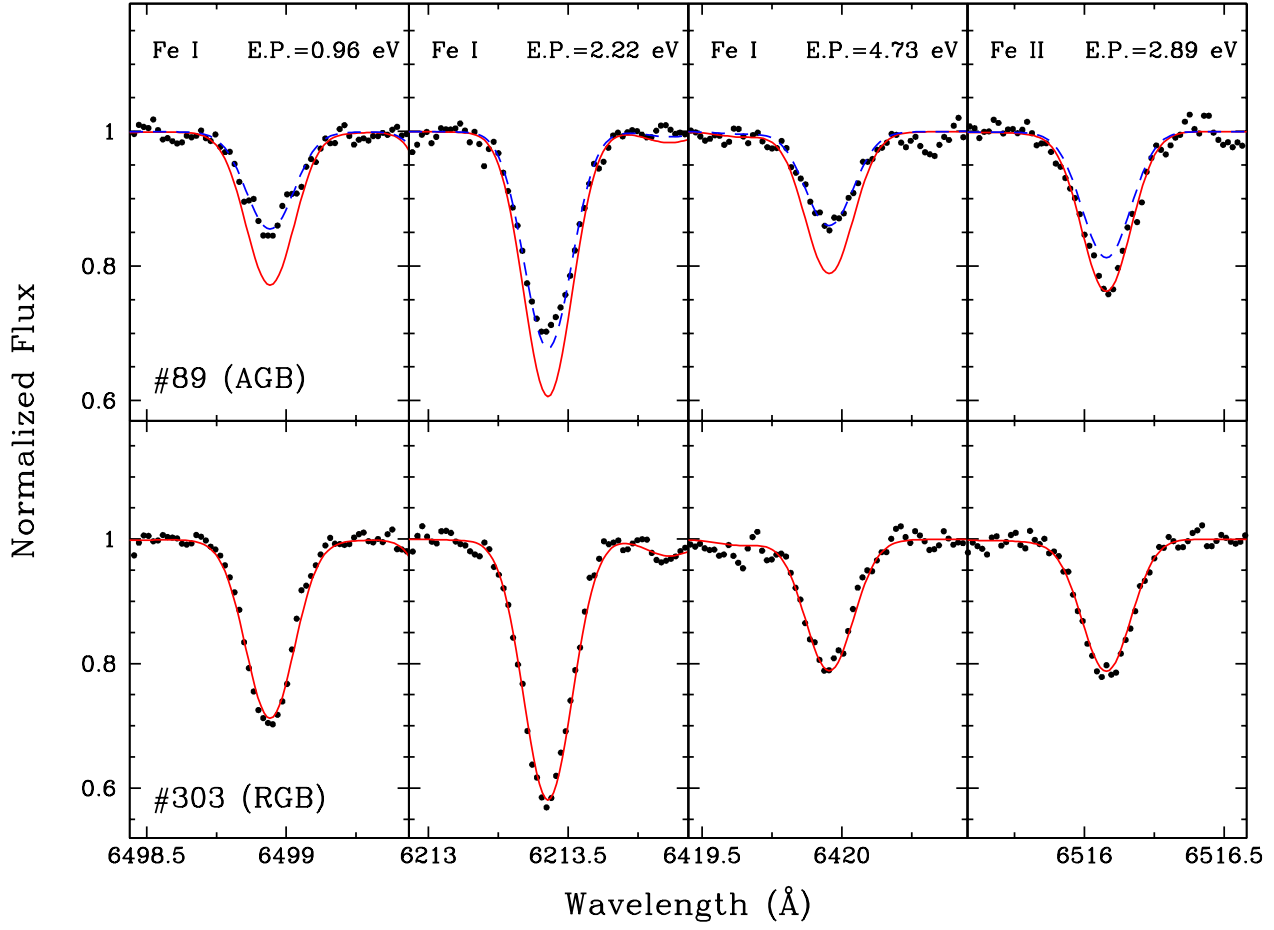


FIG. 4.— Spectral regions around three Fe I lines with different excitation potential and one Fe II line, for the AGB star #89 (upper panels) and the RGB star #303 (lower panels). Synthetic spectra calculated with the corresponding atmospheric parameters (see Table 1) and adopting the average iron abundance derived from Fe II lines are superimposed as red curves. The blue dashed curve shown in the upper panels is the synthetic spectrum calculated with the iron abundance derived from Fe I lines.